

Journal of Materials Chemistry A

Accepted Manuscript



This is an *Accepted Manuscript*, which has been through the Royal Society of Chemistry peer review process and has been accepted for publication.

Accepted Manuscripts are published online shortly after acceptance, before technical editing, formatting and proof reading. Using this free service, authors can make their results available to the community, in citable form, before we publish the edited article. We will replace this *Accepted Manuscript* with the edited and formatted *Advance Article* as soon as it is available.

You can find more information about *Accepted Manuscripts* in the [Information for Authors](#).

Please note that technical editing may introduce minor changes to the text and/or graphics, which may alter content. The journal's standard [Terms & Conditions](#) and the [Ethical guidelines](#) still apply. In no event shall the Royal Society of Chemistry be held responsible for any errors or omissions in this *Accepted Manuscript* or any consequences arising from the use of any information it contains.

Perovskite $\text{La}_{0.6}\text{Sr}_{0.4}\text{Cr}_{1-x}\text{Co}_x\text{O}_{3-\delta}$ Solid Solutions for Solar-Thermochemical Fuel Production: Strategies to Lower the Operation Temperature

A. H. Bork¹, M. Kubicek¹, M. Struzik¹, J.L.M. Rupp¹

¹) Electrochemical Materials, Department of Materials, ETH Zurich, Switzerland

Keywords: solar-to-fuel, thermochemical cycling, Strontium and cobalt doped lanthanum-chromates, perovskite, Raman, XRD,

Abstract

Storing abundant solar energy in synthetic fuels is key to ensure a sustainable energy future by replacing fossil fuels and reduce global warming emissions. Practical implementation of the solar-to-fuel technology is predicated on finding new materials with higher efficiency and lower operation temperature than state-of-the-art. We use criteria aimed for designing such efficient solar-to-fuel conversion materials in the perovskite system. Based on thermodynamic considerations first perovskite solute-solution series, $\text{La}_{0.6}\text{Sr}_{0.4}\text{Cr}_{1-x}\text{Co}_x\text{O}_{3-\delta}$, are investigated to gain fundamental understanding on the role of B-site cationic doping towards water and CO_2 splitting to synthetic fuel. Notably, all of the novel material compositions operate in a strongly lowered temperature regime of 800-1200 °C compared towards state-of-the-art binary oxides in the field. We find an optimum in doping for fuel

production performance, namely $\text{La}_{0.6}\text{Sr}_{0.4}\text{Cr}_{0.8}\text{Co}_{0.2}\text{O}_{3-\delta}$ which viably splits both CO_2 and H_2O . Based on thermogravimetric analysis, we show that highest performing perovskite splits 25 times more CO_2 compared to the current state-of-the-art material, ceria, for two-step thermochemical cycling 800-1200 °C. No adverse formation of carbonates in CO_2 atmosphere or cation segregation were observed in near and long range structural investigations, which highlight the durability and potential of these solid solutions. These new perovskite compositions enable lowering of the standard solar-to-fuel reactor temperature by 300°C. Lowered operating temperature has tremendous implications for solar-synthesized fuels in a reactor in terms of lowered heat loss, increased efficiency, and reactor materials.

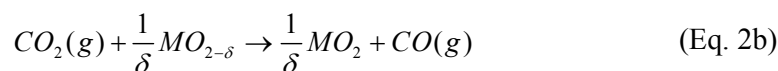
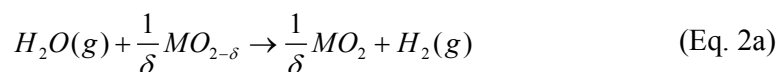
1. Introduction

The efficient use of renewable resources and transition away from dependence of fossil fuels is a global challenge of the 21st century. Energy storage and harvesting solutions beyond batteries and without restrictions on materials storage capacities are the key.^{1, 2} Today's electrochemical and photochemical energy converters and electrolysis give new promise to profit on renewable fuel production and storage in sizable-tanks with no volume restrictions. A critical element in the pursuit of this quest is the design of materials towards efficient splitting of water and carbon dioxide to hydrogen and carbon monoxide, from which storable liquid fuels can be produced. For our society, solar-synthesized chemicals and fuels are an important storable energy resource contributing to the global energy management strategies.^{3,}

In solar-to-fuel conversion, a metal oxide (ceramic) is thermally reduced in a first step by concentrated solar power and then re-oxidized in a second step by splitting CO₂ and H₂O to syngas (CO and H₂). The efficiency of the process depends on the effective oxygen stoichiometry variation of the metal oxide and its catalytic activity towards the educts. Earlier system studies of solar hydrogen production show that higher theoretical efficiencies can be achieved for two-step solar thermochemical hydrogen production compared to other techniques such as photo electrolysis or photovoltaics with electrolyser.^{5, 6} A solar driven thermochemical cycle is exemplified by a binary metal oxide in the following two-step thermochemical reactions, see Fig 1:



where MO₂ represents the binary metal oxide and the non-stoichiometry is given by δ . In a first step the metal oxide is partly reduced at the solar-driven high temperature, Eq. 1, whereby its oxygen non-stoichiometry increases. For the re-oxidation reaction, the metal oxide is exposed to water and carbon dioxide at a lowered temperature, Eqs. 2 to produce syngas (i.e. H₂ and CO)



Ceria shows promise for solar-driven thermochemical fuel production due to its stability at high temperature as well as desirable thermodynamic and kinetic characteristics.⁷ Additionally it has the highest recorded efficiency for actual on-sun testing.⁸ Despite its promise, the potential to further increase the efficiency by variation of the oxygen non-stoichiometry at lowered operation temperature is thermodynamically limited for ceria solid

solutions. Various extrinsic trivalent dopants such as Gd, Y, Sm, Sr, and Ca in ceria have been tested to improve the solar-thermochemical fuel production, but with minor effect on the solar-to-fuel efficiency⁹; in terms of defect thermodynamics (Brouwer diagrams) this is to be expected, see Mogensen¹⁰, Bishop¹¹, Wachsman¹² and Rupp^{13, 14} for details. In contrast, substitution of ceria solid solutions with smaller isovalent cations such as Zr⁴⁺ results in a remarkable increase of the defect association energy whereby the changed cerium coordination in the fluorite structure favors formation of oxygen vacancies.¹⁵⁻¹⁷ Among all tested dopants, the ceria-zirconia solid solutions reveal highest potential to increase the oxygen storage capacity.¹⁸ However, the very high operation temperature of 1500 °C needed for reduction is undesirable for reactor design, in terms of reactor material requirements and heat loss. Development of novel design principles for solar-to-fuel ceramics to operate at a lower temperature and manipulate the oxygen non-stoichiometry beyond classic binary oxides is an exciting scientific and technological goal.

As an alternative, one may consider perovskites with the ABO_{3-δ} structure as a new material class for solar-to-fuel conversion. In contrast to ceria, where vacancies are intrinsically formed at high temperatures, perovskites reported in literature rely on extrinsic acceptor doping^{19, 20}. The temperature and pO₂ dependent equilibrium shift between predominantly electronic (holes) and ionic (oxygen vacancies) p-type-defects is used as operation principle at thermal cycling. Here, both cationic sites (A- and B-site) can be doped to manipulate the oxygen non-stoichiometry, electric conductivity, kinetic and thermodynamic properties over a wider range compared to classic binary oxides.²¹⁻²³ It is due to their unique structure-oxygen non-stoichiometry relations that perovskites are high performing ceramic catalysts²⁴, memristors²⁵⁻²⁷, or electrodes for metal air batteries²⁸, oxygen separation membranes²⁹ and fuel cells³⁰⁻³². Hence, it is surprising that only recently first perovskites based on (La,Sr,Ca)MnO_{3-δ}^{20, 33, 34} and its alumina solid solutions^{35, 36} have been studied as potential

solar-to-fuel conversion reactor materials. McDaniel et al. have shown LaAlO_3 perovskites doped with Mn and Sr as promising materials for solar-to-fuel conversion due to an impressive 9 times higher H_2 yield and 6 times greater CO yield compared to the state-of-the-art binary oxide ceria in the field.³⁵ In another recent study, Demont et al. studied various classes of A- and B-site doped perovskites ($\text{ABO}_{3-\delta}$) with (A=La,Sr, B=Mn,Co,Fe) as well as $(\text{Ba,Sr})(\text{Co,Fe})\text{O}_{3-\delta}$ and their water splitting capabilities. In their comparison, $(\text{La,Sr})\text{MnO}_{3-\delta}$ showed the highest H_2 yield among the tested perovskites with 190 and 160 $\mu\text{mol/g}$ in the first and second thermochemical cycle respectively. Generally, these perovskite compositions showed high reduction yields, i.e. high oxygen release, but low re-oxidation levels during the second step of the thermochemical cycling.³⁷

Recent studies on perovskites highlight this material class as very promising for solar-to-fuel conversion, but also show a need to gain further understanding on the role of cationic doping and its implication on the fuel yields. Due to the numerous combinations of A- and B-site cationic dopants in the perovskite structure, it is imperative to have a design strategy when searching for new solar-to-fuel materials.

In this study, we screened existing literature data for a materials with a high degree of tunability towards efficient solar to fuel conversion. We synthesized the transition metal ion B-site doped $\text{La}_{0.6}\text{Sr}_{0.4}\text{Cr}_{1-x}\text{Co}_x\text{O}_{3-\delta}$ perovskite materials. The concept behind this composition is to introduce as much p-type (acceptor) doping with strontium at the A-site³⁸ for higher maximum non-stoichiometry, while staying within the limits of Sr doping for a single phase perovskite³⁹. We fix the A-site concentration and vary the B-site concentration to tune the thermodynamic properties. First, the materials are synthesized and the structure is critically investigated by X-ray diffraction analysis, Raman spectroscopy, and electron microscopy to

verify their chemical stability. Second, we assess the applicability of our design criteria by analysis of the splitting properties and fuel yields. Finally, we describe how the newly selected material composition of $\text{La}_{0.6}\text{Sr}_{0.4}\text{Cr}_{0.8}\text{Co}_{0.2}\text{O}_{3-\delta}$ produces the same amount of fuel at correspondingly 300 °C lowered operation temperatures when compared to state-of-the-art material ceria.

2. Design Criteria for Solar-to-Fuel Conversion Perovskite Materials

To design a new perovskite material for solar-to-fuel conversion we use two criteria: one criterion for each step in the two-step thermochemical reaction in order to assess the suitability of a new material, see Fig. 1. For the first step, a material criterion is a high release of oxygen for the lowest temperature possible. In the second step, a material criterion is favorable thermodynamics for H_2O and CO_2 splitting. In the following, we show how B-site doping in the solid solutions $\text{La}_{0.60}\text{Sr}_{0.40}\text{Cr}_{1-x}\text{Co}_x\text{O}_{3-\delta}$ can be tuned to fulfill the two design criteria. We demonstrate this by comparison of existing thermogravimetric data^{15, 21, 22} on $(\text{La},\text{Sr})\text{CrO}_{3-\delta}$ and $(\text{La},\text{Sr})\text{CoO}_{3-\delta}$ in the oxygen non-stoichiometry and Gibbs free energy of oxidation, Fig. 2. These thermodynamic characteristics are further compared to the ones of Zr-doped and pristine ceria, currently considered state-of-the-art material for solar to fuel conversion.

The Oxygen Release Criteria

Fig. 2a shows the effect of different B-site cations for the perovskite compositions, $\text{La}_{0.7}\text{Sr}_{0.3}\text{CrO}_{3-\delta}$ and $\text{La}_{0.7}\text{Sr}_{0.3}\text{CoO}_{3-\delta}$, in comparison to $\text{CeO}_{2-\delta}$, $\text{Ce}_{0.95}\text{Zr}_{0.05}\text{O}_{2-\delta}$ and $\text{Ce}_{0.80}\text{Zr}_{0.20}\text{O}_{2-\delta}$ on the evolution of oxygen non-stoichiometry, with respect to temperature at an exemplified oxygen partial pressure of 10^{-5} atm. The latter condition refers to a typical

value of oxygen partial pressure during thermal reduction in a solar-to-fuel reactor.^{9, 40, 41} Up to reduction temperatures of 1300°C, the perovskite $\text{La}_{0.7}\text{Sr}_{0.3}\text{CrO}_{3-\delta}$ reveals an almost invariant oxygen non-stoichiometry on temperature. In contrast, substituting with Co on the B-site to $\text{La}_{0.7}\text{Sr}_{0.3}\text{CoO}_{3-\delta}$ leads to a pronounced and increasing oxygen release, starting already at temperatures as low as 400 °C. Hence, the choice of the B-site cation, cobalt vs. chromium, implicates a remarkable difference in oxygen non-stoichiometry i.e. of $\delta = 0.16$ for 700 °C. The state-of-the-art reduction temperature for pristine and zirconia-ceria solid solutions in solar-to-fuel operation is 1500°C, for which an oxygen non-stoichiometry difference of up to $\delta = 0.04$ is measurable with respect to doping. In the plotted pO_2 and temperature range, $\text{La}_{0.7}\text{Sr}_{0.3}\text{CoO}_{3-\delta}$ reveals a 4 times increased oxygen non-stoichiometry when compared to state-of-the-art ceria-based materials at 10^{-5} atm. Consequently, the amount and temperature of release of oxygen for the perovskite can be varied to a greater extent than in commonly used ceria and zirconia-doped ceria materials.

In Fig. 2b, oxygen non-stoichiometry, δ , is plotted versus oxygen partial pressure, pO_2 , at 1000 °C. All materials displayed exhibit an increase in δ for decreasing pO_2 . We compare the equilibrium oxygen partial pressure at which the oxygen non-stoichiometry equals to $\delta = 0.1$ for the different materials: Exchange of the B-site cation from Co to Cr shifts the equilibrium pO_2 from approximately 10^{-4} to 10^{-16} atm, respectively. Thus, the equilibrium oxygen partial pressure changes by more than 12 orders of magnitude. In comparison, partial substituting of ceria by zirconia enables only a limited variation of the equilibrium oxygen partial pressure of less than 3 orders of magnitude for the same value of non-stoichiometry.

In conclusion, the temperature and equilibrium oxygen partial pressure for oxygen release can be manipulated to a much larger extent by doping the B-site in $(\text{La,Sr})\text{BO}_{3-\delta}$ with chromium and cobalt in perovskites compared to state-of-the-art ceria. Moreover, we

conclude that doping with cobalt is beneficial to tune the maximum release capacity of oxygen for the first step in the thermochemical cycling.

The Thermodynamic Material Criteria

In order to design suitable solar to fuel materials, the thermodynamic properties can be compared to determine the theoretical thermochemical conversion efficiency. However, in literature, there is not a consistent set of assumptions defining the theoretical efficiency, since this depends on the reactor type and operation. Calculations of theoretical system efficiency, result in 20% for inert gas sweeping operation^{9, 20} while it was in the excess of 30% for packed bed operation⁶ for the same material, i.e. ceria. Despite the difference in theoretical process efficiency one can assert thermodynamic suitability of new materials by a *thermodynamic criteria*. The criteria can be exemplified by considering the Gibbs free energy change for the water splitting reaction, Eq. 2a,

$$\Delta g_{rxn} = \Delta g_{oxd} - \Delta g_{H_2O} \quad (\text{Eq. 3})$$

Where Δg_{H_2O} is the Gibbs free energy of oxidation of H₂ to H₂O and Δg_{oxd} is the Gibbs free energy of oxidation of the metal oxide. In accordance, a similar expression can be defined for CO₂ splitting. When $\Delta g_{rxn} < 0$ water splitting is thermodynamically favorable and the thermodynamic criteria is fulfilled. For a more negative value of Δg_{oxd} , the *thermodynamic driving force* in reaction, Eq. 2, is larger and the chemical equilibrium shift makes the material a potentially better CO₂ and water splitter. Thermodynamic properties of H₂O and CO₂ are found in NIST-JANAF thermochemical tables.⁴² Oxidation of the metal oxides is given by the Gibbs free energy change of the oxidation reaction

$$\Delta g_{oxd} = \frac{\int_{\delta_i}^{\delta_f} \Delta g_O}{\delta_f - \delta_i} \quad (\text{Eq. 4})$$

where δ_i represents the oxygen non-stoichiometry at reduction, δ_f is the non-stoichiometry after re-oxidation. Δg_O is the molar free energy of oxidation that can be obtained from data on oxygen non-stoichiometry versus temperature and oxygen partial pressure.

In the following, we compare existing thermodynamic data to show that it is possible to tune the thermodynamic equilibrium of oxidation of the perovskites to much larger extent compared to ceria. The Gibbs free energy change, Δg_{oxd} , of the oxidation reaction is displayed for the perovskites, $\text{La}_{0.8}\text{Sr}_{0.2}\text{CrO}_{3-\delta}$ and $\text{La}_{0.8}\text{Sr}_{0.2}\text{CoO}_{3-\delta}$, and the binary oxide ceria with respect to the water-gas shift reactions of H_2 and CO oxidation and temperature, Fig. 2c. The value of Δg_{oxd} is more negative for $\text{La}_{0.8}\text{Sr}_{0.2}\text{CrO}_{3-\delta}$; viz. chromium on the B-site is thermodynamically more favorable for splitting of H_2O and CO_2 when compared to cobalt-doping for the second step of the thermochemical cycle, see Eq. 2. In addition, we conclude that it is possible to shift the Gibbs free energy of oxidation for $\text{La}_{0.8}\text{Sr}_{0.2}(\text{Cr}_{1-x}\text{Co}_x)\text{O}_{3-\delta}$ solid solutions with 150 kJ/mole by different doping at 1000 °C. Here, state-of-the-art metal oxides such as ceria and its zirconia solid solutions would restrict the range of Δg_{oxd} with approximately 60 kJ/mole.

To this end, we use two main criteria to assess the suitability of a new perovskite composition for solar-to-fuel conversion. From comparison of thermodynamic literature data on B-site doping with Co and Cr in $(\text{La,Sr})\text{BO}_{3-\delta}$, Fig. 2, it is reasonable to conclude that: (a) higher Co contents are beneficial for increased oxygen release in the first reduction step and (b) higher Cr contents are beneficial for efficient water and CO_2 splitting in the second step of the thermochemical cycle. Hence, there is a trade-off in Cr and Co doping between having a

material that has a high possible oxygen non-stoichiometry and favorable thermodynamics for syngas production. By mixing Cr and Co, the two extremes on either side of the lines of water and CO₂ splitting in Fig 2c, one can shift the thermodynamic equilibrium of oxidation of the perovskite for efficient splitting relative to different reactor temperatures. Furthermore, this comparison demonstrates how perovskites can be optimized for different reactor temperature to a higher extent compared to the state-of-the-art solar-to-fuel conversion material ceria. We have synthesized solid solution La_{0.6}Sr_{0.4}Cr_{1-x}Co_xO_{3-δ} perovskite materials, with x = 0.05, 0.10, 0.20, and 0.50 to test the predictions for mixing Cr and Co on the B-site and aim to find an optimum composition within this window of cobalt concentrations.

3. Results and Discussion

Structural Characterization of $\text{La}_{0.6}\text{Sr}_{0.4}\text{Cr}_{1-x}\text{Co}_x\text{O}_{3-\delta}$ Solid Solutions as New Solar-to-Fuel Perovskite Material.

To investigate the crystal structure and chemical stability of $\text{La}_{0.60}\text{Sr}_{0.40}\text{Cr}_{1-x}\text{Co}_x\text{O}_{3-\delta}$ compounds with $x = 0.05, 0.10, 0.20$ and 0.50 , we perform a XRD analysis of as-synthesized powders and after four thermochemical cycles, shown in Fig. 3a. The XRD patterns are characteristic for the rhombohedral structure. No impurity phases are detectable, and there are no observable indication of phase changes between the as-synthesized and thermochemically cycled materials. Lattice parameters of the unit cell for all compositions before and after cycling were determined by full profile Rietveld refinement using an $R\bar{3}c$ rhombohedral model of the unit cell. An exemplified fit for $\text{La}_{0.60}\text{Sr}_{0.40}\text{Cr}_{0.8}\text{Co}_{0.2}\text{O}_{3-\delta}$ is given in Fig. 3b. The lattice parameters for all compositions studied are plotted in Fig. 3c. A clear linear trend between the unit cell volume is observed for increasing cobalt concentration in agreement with Vegard's law. As expected a decrease in unit cell volume is observed for doping with cobalt, since cobalt ($\text{Co}^{3+}/\text{Co}^{4+}$) has smaller ionic radii compared to chromium ($\text{Cr}^{3+}/\text{Cr}^{4+}$) in octahedral coordination.⁴³

The XRD results are in agreement with literature, since similar perovskite compositions display rhombohedral symmetry^{44, 45}. The high purity phase compositions obtained through the successful Pechini process in this work are ascribed to the higher temperature and longer holding time used for synthesis compared to similar compositions where impurity phases are observed^{45, 46}.

To clarify the cation-anion near order structure relations we turn to Raman spectroscopy for the $\text{La}_{0.60}\text{Sr}_{0.40}\text{Cr}_{1-x}\text{Co}_x\text{O}_{3-\delta}$, Figure 4. The spectra exhibit two distinctive features at ~ 700 and $\sim 870 \text{ cm}^{-1}$. The as-synthesized powder samples are treated at 1200°C in air and are therefore in an oxidized state, while the thermochemically cycled powders are cooled in argon and will be in a more reduced state. The characteristics of the broad peak at $\sim 700\text{cm}^{-1}$ for the reduced $\text{La}_{0.60}\text{Sr}_{0.40}\text{Cr}_{1-x}\text{Co}_x\text{O}_{3-\delta}$ solid solutions are: (i) decreased intensity for increasing cobalt content, (ii) the peak position is shifted to lower wavenumbers for increasing cobalt content. In perovskites, this broad Raman peak signature is typically assigned to the local bending modes of oxygen in the vicinity of the B-site cation.⁴⁵⁻⁴⁷ In line with Gupta et al., we further assign this band to a mix of B_{2g} and B_{3g} Raman modes. The rhombohedral ($R\bar{3}c$) structure is confirmed by the absence of A_g modes, since Jahn-Teller distortions are incompatible with this structure type.⁴⁸ The high intensity peak at 870cm^{-1} detected for the as-synthesized (oxidized) samples are attributed to impurity phase SrCrO_4 .⁴⁶ However, this surface impurity phase is only present in some areas of the sample and it disappears after thermochemical cycling.

In summary, the structural analysis show full miscibility of Cr/Co on the B-site and all compositions can be characterized by the same rhombohedral model in both XRD and Raman spectroscopy. It can also be concluded that the materials have the same crystal structure before and after thermochemical cycling, hence displaying promise for long-term durability.

In order to study the microstructure and distribution of metal ions, scanning electron microscopy (SEM) and energy dispersive X-ray spectroscopy (EDX) is performed of the as-synthesized and thermochemically cycled $\text{La}_{0.60}\text{Sr}_{0.40}\text{Cr}_{1-x}\text{Co}_x\text{O}_{3-\delta}$ compounds with $x = 0.05, 0.10, 0.20$ and 0.50 , displayed in Fig. 5. Comparing Fig. 5a and b reveal a grain size of 0.5 to

3 μm forming agglomerated particles of approximately 50-100 μm , which is the same for the compositions $x = 0.05, 0.10,$ and 0.20 for the as-synthesized and cycled powders. However, further increase in cobalt doping to 50 mol% results in pronounced grain growth with an average grain size of 5-10 μm , Fig. 5c, which we ascribe to progressed Ostwald ripening. Ricardo et al. have shown that cobalt can be used as sintering agent to accelerate grain boundary and volume diffusion.⁴⁹ In accordance, we confirm the increased particle size and also lower number of grain facets of neighboring grains for the $\text{La}_{0.60}\text{Sr}_{0.40}\text{Cr}_{0.50}\text{Co}_{0.50}\text{O}_{3-\delta}$, Fig. 5c. We compare the microstructures of as-synthesized and thermochemically cycled $\text{La}_{0.6}\text{Sr}_{0.4}\text{Cr}_{0.8}\text{Co}_{0.2}\text{O}_{3-\delta}$ powders up to 1200 $^{\circ}\text{C}$, Fig. 5b-d. Average grain size and particle shape remain unchanged after thermochemical cycling of the material.

Energy dispersive x-ray diffraction (EDX) were performed to analyse the homogeneity of distribution of all cations, Fig. 5e,f. The analysis shows a homogeneous distribution of the metal ions throughout the sample for both, the as-synthesized and thermochemical cycled samples. Differences in concentrations of Sr and Co are related to morphological differences, see Supplementary Information S1 for further details. In essence, the results from scanning electron micrographs and chemical analysis show that the grain size and distribution of chemical elements remain unchanged from as-synthesized and after four thermochemical cycles.

Novel $\text{La}_{0.6}\text{Sr}_{0.4}\text{Cr}_{1-x}\text{Co}_x\text{O}_{3-\delta}$ Perovskite Compositions for Thermochemical Fuel Production.

Carbon Dioxide Splitting for $\text{La}_{0.6}\text{Sr}_{0.4}\text{Cr}_{1-x}\text{Co}_x\text{O}_{3-\delta}$ Perovskites

We investigate the solar-thermochemical cycling properties of $\text{La}_{0.6}\text{Sr}_{0.4}\text{Cr}_{1-x}\text{Co}_x\text{O}_{3-\delta}$ perovskite solid solutions in reduction and oxidation by splitting of CO_2 , Fig. 6. The materials are compared for four thermochemical cycles, alternating between a high

temperature step in argon and a low temperature step in a 1:1 mixture of CO₂ and argon. By varying the dopant concentration from 0.05 to 0.50 mol% in La_{0.60}Sr_{0.40}Cr_{1-x}Co_xO_{3-δ}, we vary the redox-properties of the material, Fig. 6a. Three clear trends are observed as a function of doping: First, an increase in mass loss (oxygen release) for increasing cobalt contents during the reduction step. Second, up to a cobalt dopant concentration of 20 mol% we observe a mass increase (incorporating oxygen by CO₂ splitting) during the oxidation step equivalent to the mass loss in the reduction step. However, for a high cobalt content of 50 mol% the material is re-oxidized to a lower extent. Third, we find an optimum in doping of 20 mol% of cobalt for La_{0.60}Sr_{0.40}Cr_{1-x}Co_xO_{3-δ} (x=0.2) in terms of fuel yield for the tested compositions. The trends observed in CO yield as function of doping are in agreement with design criteria and thermodynamic expectations; see Figure 2. In Fig. 2a, b it was shown that (La,Sr)BO_{3-δ} perovskite solutions with Co on the B-site are easier reduced compared to Cr, in line with the experimental results for increased cobalt content. The lower re-oxidation extent observed for high Co content (x = 0.50) is in line with presented data in Fig. 2c where we showed that the thermodynamic driving force for CO₂ splitting is lower for La_{0.8}Sr_{0.2}CoO_{3-δ} compared to La_{0.8}Sr_{0.2}CrO_{3-δ}.

The fuel production performance of the La_{0.6}Sr_{0.4}Cr_{0.8}Co_{0.2}O_{3-δ} perovskite is benchmarked towards pristine ceria, currently considered state-of-the-art material in the field of solar-to-fuel conversion, see Fig. 6b. Comparison at low temperature cycle conditions, between 800 °C (oxidation in CO₂) and 1200 °C (reduction in argon), reveals that the mass changes associated with CO₂ splitting ($\Delta m_{gain} = 0.25\%$) is 25 times higher than ceria ($\Delta m_{gain} = 0.01\%$) at the same operation conditions. We also compare the CO yield of the best performing perovskite operated at 800-1200 °C to pristine ceria operated between 1000 °C and 1500 °C. Latter high temperature cycles are commonly reported operating temperature conditions for

ceria.^{8, 9, 50} During oxidation of CeO₂ operated at high temperature we observe an almost identical mass change of 0.27 % compared to 0.25 % for La_{0.6}Sr_{0.4}Cr_{0.8}Co_{0.2}O_{3-δ} at a 300 °C lowered operation temperature. It should be noted that the profile of the mass change curve, Fig. 6b., indicates that CO production is slower for the perovskite. This either indicates that the kinetics at 800°C are slower than for ceria typically re-oxidized at 1000 °C or that the perovskite is far from equilibrium at this temperature. Interestingly, we observe a different behavior for the perovskites compared to ceria in the switch from oxidizing to reducing conditions at 800 °C, Fig. 6b. The perovskite undergoes a mass loss immediately after switching from Ar+CO₂ to Ar in contrast to ceria, where no measurable change is visible in this step. This indicates that the mass changes for the perovskite is strongly dependent on the pCO_2 . We ascribe this behavior to fast release of oxygen as a consequence of different relative pO_2 in the atmosphere. Alternative explanations for this swift mass loss are release of adsorbed CO₂ or decomposition of carbonates (e.g. SrCO₃). However, carbonate formation was excluded since it neither is detected by in-situ XRD nor by Raman spectroscopy, see also additional discussion in Supporting Information S2. For these reasons, we conclude that adsorption or carbonate formation can only have insignificant effects on the observed mass changes.

In Fig. 6c, the CO yields calculated from mass changes measured during thermochemical cycling are compared for the perovskite La_{0.6}Sr_{0.4}Cr_{1-x}Co_xO_{3-δ} solid solutions towards pristine ceria. A CO yield of 168.8 μmol/g, in Fig. 6c, for the reference measurement of undoped ceria, cycled between 1000-1500 °C, is in the range of values reported in literature 105 μmol/g⁵⁰ and 193 μmol/g²⁰ at similar operation conditions. As additional comparison the Mn- and Sr- doped LaAlO₃ based perovskites had a CO production with an average of 135 μmol/g over 80 cycles between 1000-1350°C in a stagnating flow reactor.

For supplementary verification of CO₂ splitting, we measure the fuel production yields by non-dispersive infrared sensors for the material with highest performance, La_{0.6}Sr_{0.4}Cr_{0.8}Co_{0.2}O₃, in a fluidized bed reactor. Figure 7 shows the amount of produced CO as a function of time for two different cycles, the time of injection of CO₂ is marked with a grey square. Owing to a lower reduction temperature longer reduction times were needed to reach higher non-stoichiometries. In the first cycle the material was reduced for 1 hour and in the second it was reduced for 4 hours. For the second cycle it will have a higher non-stoichiometry and as expected we see a higher yield of CO. The yields were 10 μmol/g and 63 μmol/g for the first and second cycle respectively. The fact that the CO₂ concentration is 1:3 in inert gas compared to 1:1 in the thermogravimetric measurements and that the reduction temperature was 200 °C lower (reduction at 1200 °C in TGA experiments) reasonably account for the lower fuel yield.

CO₂ and water splitting to syngas by the best performing perovskite La_{0.6}Sr_{0.4}Cr_{0.8}Co_{0.2}O_{3-δ}

In Figure 8, we demonstrate carbon dioxide and water splitting with the best performing perovskite La_{0.6}Sr_{0.4}Cr_{0.8}Co_{0.2}O_{3-δ} by thermogravimetric measurements. Here, the mass changes arising from incorporation of oxygen by water splitting and carbon dioxide are compared. Calculation of the fuel yield is determined from the three reproducible cycles 2-4, ignoring the first cycle, which typically differs significantly from the following cycles.^{37, 50} We observe a relative mass change of 0.08 % and 0.25% during oxidation by H₂O and CO₂ respectively. This corresponds to a H₂ yield of 50 μmol/g and a CO yield of 157 μmol/g. The lower mass gain during water splitting compared to carbon dioxide splitting for the perovskite is attributed to the educts' lower relative water concentration (2.5% H₂O in argon) compared to gaseous carbon dioxide (50% CO₂ in argon). Additionally, the difference in H₂ and CO yield may be ascribed to the perovskites different reactivity towards water and CO₂

splitting as observed by McDaniel et al.³⁵ Interestingly, we observe that the mass gain for water splitting occur in two steps, first by a fast reaction, then by a reaction with slower kinetics.

In real solar-to-fuel reactors the overall process efficiency is of high importance for the viability of a material. For this model system, the thermogravimetric measurements reveal an optimum in doping with respect to fuel production. However, the composition with the highest fuel yield is not necessarily the composition with the highest efficiency. Determining process efficiency is a complex procedure determined by reactor design and operation. For example, Scheffe and co-workers raised concern about a lowered efficiency for $(\text{La,Sr})\text{MnO}_{3-\delta}$ perovskites compared to ceria because they require higher amounts of oxidants (H_2O and CO_2) leading to energy penalties in form of heat loss.²⁰ Yet, Ermonoski et al. showed that a smart design of the solar-to-fuel reactor enables a higher heat recovery making it possible to work with higher educt concentration.⁶ This makes materials with lower Gibbs free energy of oxidation, Δg_{oxd} , and lower operating temperature than ceria more attractive. It is beyond the scope of this paper to determine the theoretical efficiency, since this requires a determination of the thermodynamic properties for all compositions in a wide pO_2 and temperature range.^{6, 9, 18} To this point, we have shown that the solid solution series $\text{La}_{0.6}\text{Sr}_{0.4}\text{Cr}_{1-x}\text{Co}_x\text{O}_{3-\delta}$ has a potential to replace the best performing materials because the thermodynamic properties can be tailored to a larger extent compared to materials known in the field of solar-to-fuel conversion.

We conclude that the perovskite has a CO production of $157\mu\text{mol/g}$ even when operated at a lowered temperature cycle of $800\text{-}1200\text{ }^\circ\text{C}$, compared to a CO yield of $168\text{ }\mu\text{mol/g}$ for ceria operated at $1000\text{-}1500\text{ }^\circ\text{C}$. Thus, we report an almost equivalent fuel yield to state-of-the-art material at $300\text{ }^\circ\text{C}$ lower operating temperature. Additionally, the large variation in fuel yield

of 14 $\mu\text{mol/g}$ to 157 $\mu\text{mol/g}$ depending on concentration of cobalt on the B-site, shows that the thermodynamic properties are highly dependent on the doping. A high degree of tuneability of thermodynamic properties is beneficial when optimizing for system efficiency.

Structural Stability of $\text{La}_{0.6}\text{Sr}_{0.4}\text{Cr}_{0.8}\text{Co}_{0.2}\text{O}_{3-\delta}$ Perovskites for Solar-to-Fuel Conversion: In-situ Carbon Dioxide Redox-Cycling

Promising fuel yields from H_2O and CO_2 splitting have been demonstrated for $\text{La}_{0.6}\text{Sr}_{0.4}\text{Cr}_{0.8}\text{Co}_{0.2}\text{O}_{3-\delta}$. At this point, it may be debated that the weight gains measured by thermogravimetric analysis are not only related to splitting of CO_2 but also formation of Sr- or La-carbonates. Secondary phases and strontium carbonate formation have previously been detected by in-situ XRD in perovskites with Sr on the A-site in $\text{La}(\text{Co,Fe})\text{O}_{3-\delta}$ -compositions when exposed to CO_2 in the temperature range 550-1000 °C.^{51, 52} Phase changes or carbonate formation may lead to degradation and decrease in performance over time.⁵³ To clarify the structural stability and possible carbonate formation, we performed in-situ X-ray powder diffraction analysis for the best performing perovskite $\text{La}_{0.6}\text{Sr}_{0.4}\text{Cr}_{0.8}\text{Co}_{0.2}\text{O}_{3-\delta}$ material under redox reaction with carbon dioxide. In Figure 9, in-situ X-ray diffraction data are displayed for $\text{La}_{0.6}\text{Sr}_{0.4}\text{Cr}_{0.8}\text{Co}_{0.2}\text{O}_{3-\delta}$ for a temperature of 1200 °C and 800 °C. At the lower temperature of 800 °C the sample was exposed to argon and a mix of 5 vol% CO_2 in Ar for 5 hours. This temperature and atmosphere program was used to reproduce the instantaneous changes the sample is exposed to during a solar-thermochemical cycle and enable investigation of long-term effects of exposure to CO_2 . In Fig. 9a, we show XRDs displaying the main peaks of (012) and the doublets of (110) and (104); a close up of the double peak (110) and (104) is displayed in Fig. 9b. By analyses of the redox-characteristics (under oxidation by CO_2 and reduction in argon) we unequivocally show that there is neither changes of the peak shape

over time nor additional diffraction lines. A slight shift of the (110) peak is related to the chemical expansion due to incorporation of oxygen by CO₂ splitting.^{54, 55}

In this study, we clearly confirm that the material La_{0.6}Sr_{0.4}Cr_{0.8}Co_{0.2}O_{3-δ} is able to split carbon dioxide and water with a larger promise than state-of-the-art ceria. Through in-situ structural redox-experiments we prove that it is stable in a carbon dioxide atmosphere and that intermediate carbonate formations are not to be accounted for the time tested. This is supported by fact that the carbonate vibration structural bands, e.g. characteristic SrCO₃ bands at the wavenumber ~1071cm⁻¹^{56, 57}, are not traceable in our Raman experiments after thermochemical cycling of the materials.

4. Conclusion

In this work, we report for the first time that the material $\text{La}_{0.6}\text{Sr}_{0.4}\text{Cr}_{1-x}\text{Co}_x\text{O}_{3-\delta}$ reveals a high potential to replace state-of-the-art ceria, due to its ability to split carbon dioxide and water as new solar-to-fuel conversion reactor material at lower temperature.

Ceria is currently considered state-of-the-art material in solar-driven thermochemical dissociation of CO_2 and H_2O due to favorable thermodynamics and kinetic characteristics. By thermogravimetric analysis we find a comparably high performing perovskite material, namely $\text{La}_{0.6}\text{Sr}_{0.4}\text{Cr}_{0.8}\text{Co}_{0.2}\text{O}_{3-\delta}$, in the temperature range 800 °C-1200 °C even strongly outperforming ceria with a 25 times greater CO yield compared to ceria (800-1200 °C). A comprehensive structural ex- and in-situ study under harsh conditions, such as simulated carbon dioxide heat redox-cycle, show no sign of phase changes or carbonate formation for potential reactor operation. The fact that the material can be operated at a strongly lowered temperature implies that heat losses and overall material temperature gradients during solar-driven heating can be minimized. Potential operation at higher temperature regime may be evaluated for further efficiency increase due to the high oxygen storage capacity of the material.

The novel material was chosen based on evaluation of existing thermodynamic data on $(\text{La,Sr})\text{CrO}_{3-\delta}$ and $(\text{La,Sr})\text{CoO}_{3-\delta}$ with a criteria of release of oxygen at low temperature as well as favorable thermodynamic characteristics for water and CO_2 splitting. By this comparison we demonstrate that the oxygen non-stoichiometry and thermodynamic properties of B-site doped $(\text{La,Sr})\text{BO}_{3-\delta}$ solid solutions can be varied to a much larger extent than for example ceria. The present work contributes with first model material experiments for which solid solution series have been synthesized to systematically investigate the effect

on structure, chemistry and thermochemical syngas production for the series of $\text{La}_{0.6}\text{Sr}_{0.4}\text{Cr}_{1-x}\text{Co}_x\text{O}_{3-\delta}$. We exploit the significant variations in oxygen non-stoichiometry and thermodynamic properties to optimize fuel yields. Based on the material's insights we show that there is a trade-off in doping: cobalt doping increases the release of oxygen in the 1st high temperature reducing step, but it comes at the price of a less favorable thermodynamics for CO_2 and water splitting at the 2nd low temperature step. The fact that the thermodynamic properties of the solid solution series can be tuned to this extent, while maintaining structural integrity, makes it interesting for real solar-to-reactor systems. We anticipate that further studies of the thermodynamic properties can be used to find an optimum composition within this solid solution series for high process efficiency depending on the reactor type and operation.

5. Methods

Material Synthesis

Solid solutions of $\text{La}_{0.60}\text{Sr}_{0.40}\text{Cr}_{1-x}\text{Co}_x\text{O}_{3-\delta}$ (with $x=0.05, 0.10, 0.20, 0.50$) were synthesized as powders via the Pechini method. For this, stoichiometric quantities of the metal nitrates, being $\text{La}(\text{NO}_3)_3 \cdot 6\text{H}_2\text{O}$ (Fluka Analytical, $\geq 99\%$), $\text{Sr}(\text{NO}_3)_2$ (Fluka Analytical $\geq 99\%$), $\text{Cr}(\text{NO}_3)_3 \cdot 9\text{H}_2\text{O}$ (Sigma-Aldrich $\geq 99\%$) and $\text{Co}(\text{NO}_3)_2 \cdot 6\text{H}_2\text{O}$ (Fluka Analytical, $\geq 98\%$) were mixed with a molar ratio of 60/40 with citric acid (Sigma-Aldrich, $\geq 99\%$) under continuous stirring at room temperature. Hereby, an excess of citric acid is used to ensure complexation of the metal cations. Ethylene glycol (Fluka Analytical, $\geq 99.5\%$) was added to the citric acid in a 2/3 wt. ratio. The solution was heated until a gel was formed and then calcined at $400\text{ }^\circ\text{C}$ for 2h to evaporate the organic residues. The resulting powder was grinded and heat treated at $1200\text{ }^\circ\text{C}$ for 24 hours, with a heating rate of $2\text{ }^\circ\text{C}/\text{min}$, to acquire a single-phase powder and to assure the chemical stability prior to thermogravimetric measurements.

Structural and Chemical Analysis.

Long-range cationic structure investigation

X-ray powder diffraction data were collected in flat plate θ/θ geometry at ambient temperature with a Panalytical Empyrean X-ray diffractometer, equipped with a PIXcel1D detector, using Ni filtered Cu K_α radiation ($\lambda_1 = 1.540598\text{ \AA}$, $\lambda_2 = 1.544426\text{ \AA}$). XRD data were collected in the 2θ -range of 15° to 110° , with an effective step width of 0.0131° and a scan time of 170 sec. per step.

In-situ XRD experiments at elevated temperatures were performed using Panalytical X'Pert Pro diffractometer equipped with an X'Celerator detector and with an Anton-Paar HTK 1200

high temperature furnace with controlled atmosphere. A constant total flow rate of 200 sccm was used for both reduction (argon) and oxidation (argon+CO₂) step. In the oxidation step the CO₂ concentration had to be chosen lower (5% in argon) in the in-situ XRD compared to the thermogravimetric measurements (50% CO₂ in argon) due to experimental limitations of the XRD setup. Data were collected at 1200°C and 800°C over the range $2\theta=20-60^\circ$, in steps of 0.0167° , with an effective scan time of 40 s per step and equilibration time of 30 min. between measurements.

The unit cell parameters were determined by Rietveld whole profile fitting of the recorded ex-situ XRD data using the program GSAS.⁵⁸ A rhombohedral unit cell model for the space group $R\bar{3}c$ was successfully used for all refinements.⁵⁹ In this structural fit arrangement the cations were located on ideal structural sites, specifically (using Wyckoff nomenclature) the $6a$ sites (0, 0, $\frac{1}{4}$) for the La and Sr and the $6b$ sites (0 0 0) for the Co and Cr. The anionic oxide positions were fixed for the $8e$ crystallographic sites (z 0 $\frac{1}{4}$) with $z = 0.54$.

Near order oxygen anionic-cationic lattice characterisations

Raman spectra were collected using a confocal WITec CRM200 Raman microscope instrument (WITec Germany) equipped with a 452 nm wavelength laser for excitation and spectral resolution of 0.7 cm^{-1} . Additional experiments were conducted with a 633 nm wavelength laser but this resulted in fluorescence.

Microstructure and chemistry

The materials' morphology and chemistry were characterized by a scanning electron microscope and the distribution of chemical elements were locally resolved by Energy Dispersive X-ray spectroscopy (LEO 1530, SEM).

Thermochemical Measurements.

The thermochemically driven oxygen non-stoichiometry changes of $\text{La}_{0.60}\text{Sr}_{0.40}\text{Cr}_{1-x}\text{Co}_x\text{O}_{3-\delta}$ materials were studied in a thermogravimetric analyzer (TGA, NETZSCH 449C) for temperature and gas environment cycling. For each measurement, 200 mg of powder were placed in Al_2O_3 TGA-crucibles (NETZSCH) and cycled between 800 and 1200 °C, with heating rates of 50 °C/min., and a total flow of 100 sccm. For reduction and oxidation high purity Ar (Pangas, 99.999 %) and CO_2 (99.9 %) were mixed. During oxidation 50% CO_2 in Ar, and 100 % Ar during reduction. For the oxidation step, we use an isotherm of 1h at 800 °C, with 10 min. equilibration in reducing atmosphere before and after oxidation in CO_2 . Gas flows and timescale of the thermochemical experiments were chosen to enable a performance assessment of the proposed perovskite materials towards other materials in earlier thermogravimetric studies for similar conditions.^{20, 50, 60} Moreover, the conditions resemble reactor operation demonstrated by Chueh et al.⁸ with on-sun simulated operation. Granting, in the simulated reactor operation lower gas flows were used (0.035L/min/g) compared to previous thermogravimetric evaluations and this one (0.25L/min/g).

To exclude buoyancy effects, experimental runs were carried out under equivalent conditions in the same and empty crucibles for the thermogravimetric measurement. In Fig. 5a, b the relative mass is set to zero at the beginning of the re-oxidation step to ease comparison of CO-yield between compositions. The relative mass change measured by thermogravimetry at the re-oxidation step under the CO_2 flow is converted to CO yield, n_{CO} , which is given by

$$n_{\text{CO}} = \frac{\Delta m_{\text{gain}}}{M_{\text{O}} m_{\text{perovskite}}} \quad (\text{Eq. 5})$$

Where Δm_{gain} is the mass increase during the oxidation step, M_O is the molecular weight of oxygen, and $m_{\text{perovskite}}$ is the mass of the sample.

We compare the oxygen deficiencies and CO₂/Ar cycling kinetics of the best performing La_{0.6}Sr_{0.4}Cr_{0.8}Co_{0.2}O_{3- δ} perovskite in this study to the state-of-the-art in the field being CeO_{2- δ} (Cerac, 99.9 %). For this, thermochemical cycling was either studied at a low temperature range of 800 to 1200 °C with a heating rates of 50 °C/min, or for a high temperature range of 1000-1500 °C with a 20 °C/min heating rate. We depicted on purpose these conditions, since the first low temperature thermochemical cycling would be a range where we expected sufficient oxygen release from the perovskite, Fig. 2a, b, whereas the higher one is the state-of-the-art operation range for solar-to-fuel conversion on the binary oxide ceria.^{8, 9, 50}

Water splitting experiments were carried out by flushing argon through a water bubbler before entering the TGA. The temperature of the water was kept at 21 °C, thus we obtain a water vapor pressure of $p_{H_2O} = 2.5$ atm or a concentration of 2.5 % in argon.

Fuel production measurements in fluidized bed reactor

To confirm CO₂ splitting by the perovskite solution La_{0.6}Sr_{0.4}Cr_{0.8}Co_{0.2}O_{3- δ} we detect and quantify the amount of produced CO by an infrared sensor in a fluidized bed reactor. The setup is described elsewhere.⁶¹ In the two-step thermochemical experiment, reduction and oxidation was performed at 1000 and 800 °C respectively. The lower reduction temperature in this experiment compared to the thermogravimetric analysis was used due to limitations on the upper temperature of the setup. The flow was 1.5 L/min of N₂ during reduction. During the oxidation step the flows were 1.5 L/min of N₂ and 0.5 L/min of CO₂. The perovskite powders were synthesized as described above and subsequently pressed into pellets, crushed and sieved to a particle size range of 300-425 μm . Alumina particles were used as fluidized bed.

6. Acknowledgements

The authors want to thank Prof. A. Studart from the Laboratory of Complex Materials for the use of the TGA and SEM. Prof. R. Spolenak from the Laboratory for Nanometallurgy for use of the Raman spectrometer and Prof. M. Niederberger from the Laboratory for Multifunctional Materials for the use of the XRD facilities and a special thanks to D. Erdem for support with high temperature in-situ XRD measurements (ETH Zurich, Switzerland). Prof. C. Müller and Q. Imtiaz are gratefully acknowledged for measurements in the fluidized bed reactor (ETH Zurich, Switzerland). Furthermore, the authors thank S. Schweiger and R. Schmitt for assistance with Raman Spectroscopy and SEM measurements respectively. We also thank the partners of Competence Center for Energy and Mobility (CCEM-CH) for valuable discussions. Funding support by ETH, grant number ETH-05 13-1, is gratefully acknowledged.

7. References

1. I. Lubomirsky. and D. Cahen, *MRS Bulletin*, 2012, 37, 412-416.
2. D. S. Ginley and D. Cahen, *Fundamentals of materials for energy and environmental sustainability*, Cambridge university press, 2011.
3. A. Yilanci, I. Dincer, and H. K. Ozturk, *Progress in Energy and Combustion Science*, 2009, 35, 231-244.
4. T. Kodama and N. Gokon, *Chemical Reviews*, 2007, 107, 4048-4077.
5. R. B. Diver, J. E. Miller, M. D. Allendorf, N. P. Siegel and R. E. Hogan, *Journal of Solar Energy Engineering*, 2008, 130, 041001.
6. I. Ermanoski, N. P. Siegel and E. B. Stechel, *Journal of Solar Energy Engineering*, 2013, 135, 031002.
7. W. C. Chueh and S. M. Haile, *Philosophical Transactions of the Royal Society A: Mathematical, Physical and Engineering Sciences*, 2010, 368, 3269-3294.
8. W. C. Chueh, C. Falter, M. Abbott, D. Scipio, P. Furler, S. M. Haile and A. Steinfeld, *Science*, 2010, 330, 1797-1801.
9. J. R. Scheffe and A. Steinfeld, *Energy & Fuels*, 2012, 26, 1928-1936.
10. M. Mogensen, N. M. Sammes and G. A. Tompsett, *Solid State Ionics*, 2000, 129, 63-94.
11. S. Bishop, K. Duncan and E. Wachsman, *Electrochimica Acta*, 2009, 54, 1436-1443.
12. S. Omar, E. Wachsman, J. L. Jones and J. Nino, *J Am Ceram Soc*, 2009, 92, 2674-2681.
13. J. L. M. Rupp, A. Infortuna and L. J. Gauckler, *Journal of the American Ceramic Society*, 2007, 90, 1792-1797.
14. J. L. M. Rupp, E. Fabbri, D. Marrocchelli, J. W. Han, D. Chen, E. Traversa, H. L. Tuller and B. Yildiz, *Advanced Functional Materials*, 2014, 24, 1562-1574.
15. M. Kuhn, S. Bishop, J. L. M. Rupp and H. Tuller, *Acta Materialia*, 2013, 61, 4277-4288.
16. D. Chen, Y. Cao, D. Weng and H. L. Tuller, *Chemistry of Materials*, 2014, 26, 5143-5150.
17. J. P. Eufinger, M. Daniels, K. Schmale, S. Berendts, G. Ulbrich, M. Lerch, H. D. Wiemhöfer and J. Janek, *Physical Chemistry Chemical Physics*, 2014, 16, 25583-25600.
18. Y. Hao, C. K. Yang and S. M. Haile, *Chemistry of Materials*, 2014, 26, 6073-6082.
19. A. McDaniel, A. Ambrosini, E. Coker, J. Miller, W. Chueh, R. O'Hayre and J. Tong, *Energy Procedia*, 2014, 49, 2009-2018.
20. J. R. Scheffe, D. Weibel and A. Steinfeld, *Energy & Fuels*, 2013, 27, 4250-4257.
21. J. Mizusaki, Y. Mima, S. Yamauchi, K. Fueki and H. Tagawa, *Journal of Solid State Chemistry*, 1989, 80, 102-111.
22. J. Mizusaki, S. Yamauchi, K. Fueki and A. Ishikawa, *Solid State Ionics*, 1984, 12, 119-124.
23. M. Oishi, K. Yashiro, K. Sato, J. Mizusaki and T. Kawada, *Journal of Solid State Chemistry*, 2008, 181, 3177-3184.
24. H. Falcon, J. Barbero, J. Alonso, M. Martínez-Lope and J. Fierro, *Chemistry of materials*, 2002, 14, 2325-2333.
25. F. Messerschmitt, M. Kubicek, S. Schweiger and J. L. M. Rupp, *Advanced Functional Materials*, 2014, 24, 7447-7447.
26. M. Kubicek, R. Schmitt, F. Messerschmitt and J. L. M. Rupp, Submitted 2015.
27. F. Messerschmitt, M. Kubicek and J. L. M. Rupp, Submitted, 2015.
28. J. Suntivich, H. A. Gasteiger, N. Yabuuchi, H. Nakanishi, J. B. Goodenough and Y. Shao-Horn, *Nature chemistry*, 2011, 3, 546-550.
29. P. V. Hendriksen, P. H. Larsen, M. Mogensen, F. W. Poulsen and K. Wiik, *Catalysis Today*, 2000, 56, 283-295.
30. U. P. Muecke, D. Beckel, A. Bernard, A. Bieberle-Hütter, S. Graf, A. Infortuna, P. Müller, J. L. M. Rupp, J. Schneider and L. J. Gauckler, *Advanced Functional Materials*, 2008, 18, 3158-3168.
31. E. D. Wachsman and K. T. Lee, *Science*, 2011, 334, 935-939.

32. A. S. Harvey, F. J. Litterst, Z. Yang, J. L. M. Rupp, A. Infortuna and L. J. Gauckler, *Physical Chemistry Chemical Physics*, 2009, 11, 3090-3098.
33. C.-K. Yang, Y. Yamazaki, A. Aydin and S. M. Haile, *Journal of Materials Chemistry A*, 2014, 2, 13612-13623.
34. S. Dey, B. Naidu and C. Rao, *Chemistry-A European Journal*, 2015, 21, 7077-7081.
35. A. H. McDaniel, E. C. Miller, D. Arifin, A. Ambrosini, E. N. Coker, R. O'Hayre, W. C. Chueh and J. Tong, *Energy & Environmental Science*, 2013, 6, 2424-2428.
36. A. M. Deml, V. Stevanović, A. M. Holder, M. Sanders, R. O'Hayre and C. B. Musgrave, *Chemistry of Materials*, 2014, 26, 6595-6602.
37. A. Demont, S. Abanades and E. Beche, *The Journal of Physical Chemistry C*, 2014.
38. H. U. Anderson, M. Nasrallah, B. Flandermeyer and A. Agarwal, *Journal of Solid State Chemistry*, 1985, 56, 325-334.
39. P. S. Devi and M. S. Rao, *Journal of Solid State Chemistry*, 1992, 98, 237-244.
40. M. Romero and A. Steinfeld, *Energy & Environmental Science*, 2012, 5, 9234-9245.
41. A. Steinfeld, *Solar energy*, 2005, 78, 603-615.
42. M. W. Chase and J. A. N. A. Force, 1998.
43. R. D. Shannon, *Acta Crystallographica Section A: Crystal Physics, Diffraction, Theoretical and General Crystallography*, 1976, 32, 751-767.
44. M. Anzai, H. Kawakami, T. Takayama and H. Yamamura, *Transactions of the Materials Research Society of Japan*, 2010, 35, 503-506.
45. M. Mori, Y. Hiei and N. M. Sammes, *Solid State Ionics*, 2000, 135, 743-748.
46. R. K. Gupta and C. M. Whang, *Journal of Physics: Condensed Matter*, 2007, 19, 196209.
47. D. Hoang, A. Dittmar, M. Schneider, A. Trunschke, H. Lieske, K.-W. Brzezinka and K. Witke, *Thermochimica acta*, 2003, 400, 153-163.
48. M. N. Iliev and M. V. Abrashev, *Journal of Raman Spectroscopy*, 2001, 32, 805-811.
49. R. Polini, A. Falsetti, E. Traversa, O. Schäf and P. Knauth, *Journal of the European Ceramic Society*, 2007, 27, 4291-4296.
50. A. Le Gal, S. Abanades and G. Flamant, *Energy & Fuels*, 2011, 25, 4836-4845.
51. V. Esposito, M. Søgaard and P. V. Hendriksen, *Solid State Ionics*, 2012, 227, 46-56.
52. S. Rajesh, J. Pereira, F. Figueiredo and F. Marques, *Electrochimica Acta*, 2014, 125, 435-442.
53. M. Gálvez, R. Jacot, J. Scheffe, T. Cooper, G. Patzke and A. Steinfeld, *Physical Chemistry Chemical Physics*, 2015, 17, 6629-6634.
54. J. Ovenstone, J. S. White and S. T. Mixture, *Journal of Power Sources*, 2008, 181, 56-61.
55. N. H. Perry, S. R. Bishop and H. L. Tuller, *Journal of Materials Chemistry A*, 2014, 2, 18906-18916.
56. M. C. Alves, M. R. Nascimento, S. J. Lima, P. S. Pizani, J. W. Espinosa, E. Longo, L. E. Soledade, A. G. Souza and I. M. Santos, *Materials Letters*, 2009, 63, 118-120.
57. N. Eror, T. Loehr and U. Balachandran, *Ferroelectrics*, 1982, 40, 71-73.
58. A. C. Larson and R. B. v. Dreele, *Los Alamos National Laboratory Report LAUR 86-748*, 2004.
59. R. Sonntag, S. Neov, V. Kozhukharov, D. Neov and J. Ten Elshof, *Physica B: Condensed Matter*, 1997, 241, 393-396.
60. A. Demont and S. Abanades, *Journal of Materials Chemistry A*, 2015.
61. Q. Imtiaz, A. M. Kierzkowska, M. Broda and C. R. Müller, *Environmental science & technology*, 2012, 46, 3561-3566.

2-Step Thermochemical Solar-to-Fuel Conversion

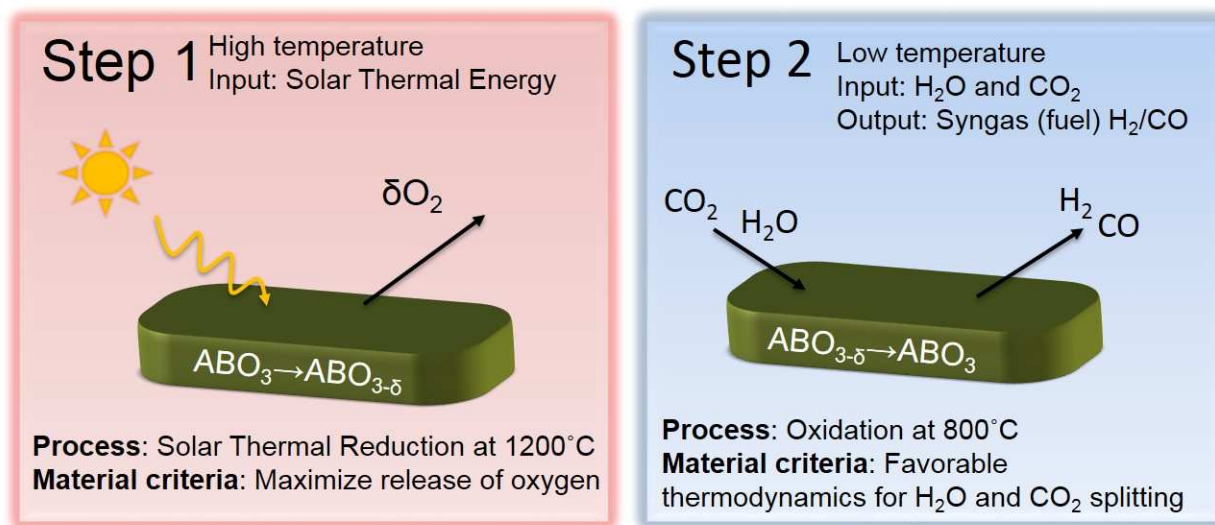


Figure 1. Schematic of 2-step thermochemical solar-to-fuel conversion process. In the first step, the perovskite, with the structure $ABO_{3-\delta}$, is thermally reduced up to a non-stoichiometry, δ . In the second step, the perovskite is re-oxidized by splitting H_2O and CO_2 . A material search criterion for the first step is a high release of oxygen at the lowest temperature possible while it is favorable thermodynamics for H_2O and CO_2 splitting in the second step.

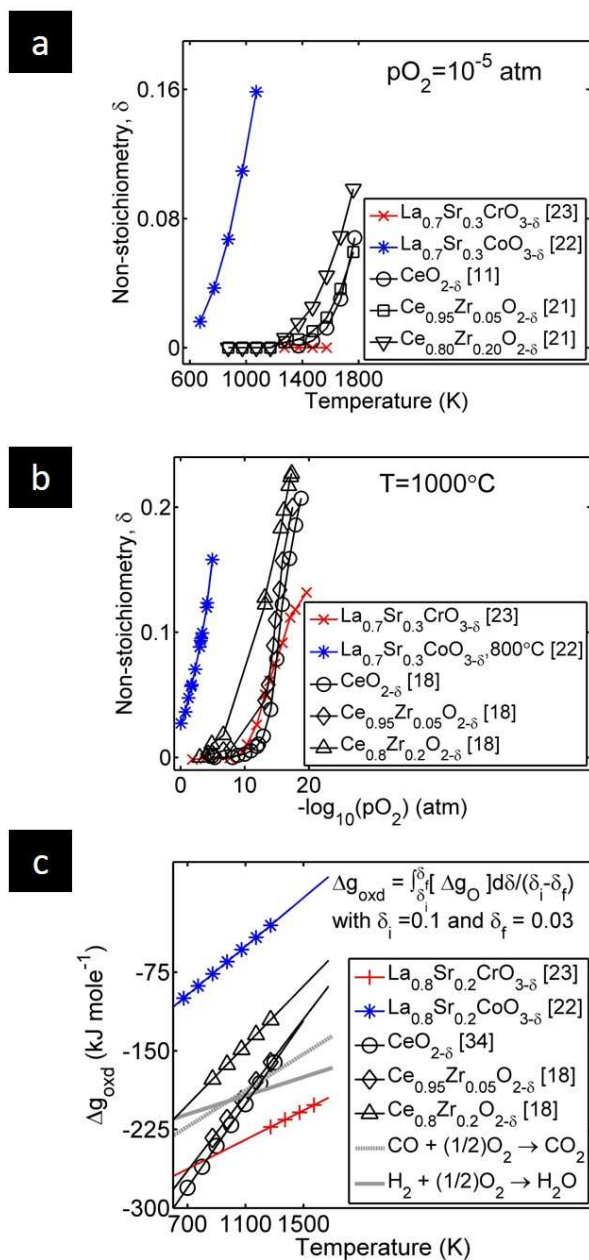


Figure 2. Existing literature data on $(La,Sr)BO_{3-\delta}$ along with doped and pristine ceria to compare the impact of two different B-site cationic dopants: Cr and Co. a) Non-stoichiometry vs. temperature for B-site doped $La_{0.7}Sr_{0.3}BO_{3-\delta}$ compared to zirconia-doped ceria and pristine ceria at a constant oxygen partial pressure of $pO_2 = 10^{-5}$ atm. Solid lines are used to guide the eye. b) Equilibrium non-stoichiometry vs pO_2 for B-site doped $La_{0.7}Sr_{0.3}BO_{3-\delta}$ zirconia-doped ceria and pristine ceria compared at a temperature of 1000°C . The solid lines are used as guidance to the eye. c) Gibbs free energy of oxidation, Δg_{oxd} , of doped perovskites compared to ceria and to the water and gas shift reaction, of relevance for the solar-to-fuel conversion, for different temperatures. The calculation of Δg_{oxd} is done by integration of the oxygen molar free energy, Δg_{O} , for the respective materials over a realistic non-stoichiometry range: for the initial non-stoichiometry of $\delta_i = 0.1$ to a final non-stoichiometry of $\delta_f = 0.03$. Point-markers represent the temperature range of the respective experiments and solid lines represent linear inter- and extrapolation. Information on water and CO_2 splitting is derived from NIST-JANAF thermochemical tables.

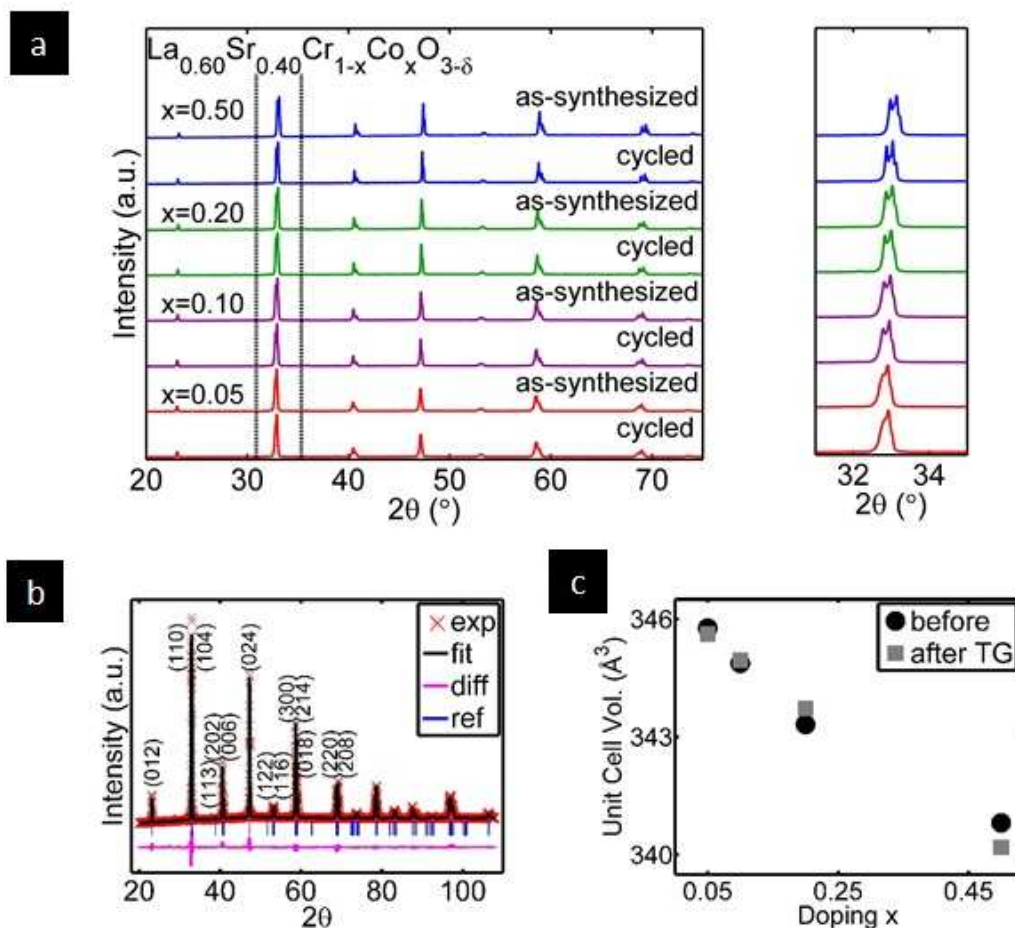


Figure 3. X-ray powder diffraction patterns of $\text{La}_{0.6}\text{Sr}_{0.4}\text{Cr}_{1-x}\text{Co}_x\text{O}_{3-\delta}$ with respect to solid solution doping before (as-synthesized) and after thermochemical cycling (cycled) for the temperature range of 800 to 1200°C. a) Entire measured range and dashed lines indicate narrow range to the right. b) Fitted X-ray diffraction profile for $\text{La}_{0.6}\text{Sr}_{0.4}\text{Cr}_{0.8}\text{Co}_{0.2}\text{O}_{3-\delta}$. Experimental data (exp), calculated (fit), and difference (diff) profiles are shown with reflection positions indicated by markers (ref). c) Rhombohedral unit cell volume plotted as a function of B-site doping with cobalt. Errorbars are within the size of the symbol marker.

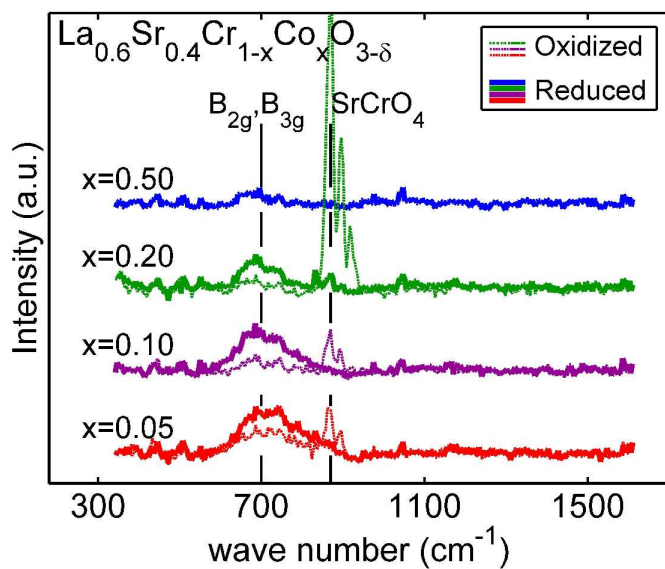


Figure 4. Raman Spectra of $\text{La}_{0.6}\text{Sr}_{0.4}\text{Cr}_{1-x}\text{Co}_x\text{O}_{3-\delta}$ with $x=0.05, 0.10, 0.20,$ and 0.50 for as-synthesized (oxidized) and thermochemically cycled powders (reduced). Broad peak at $\sim 700\text{cm}^{-1}$ is assigned to B_{2g} and B_{3g} breathing modes. The feature at 870cm^{-1} visible only for some spots in the oxidized samples are assigned to impurity phase SrCrO_4 .

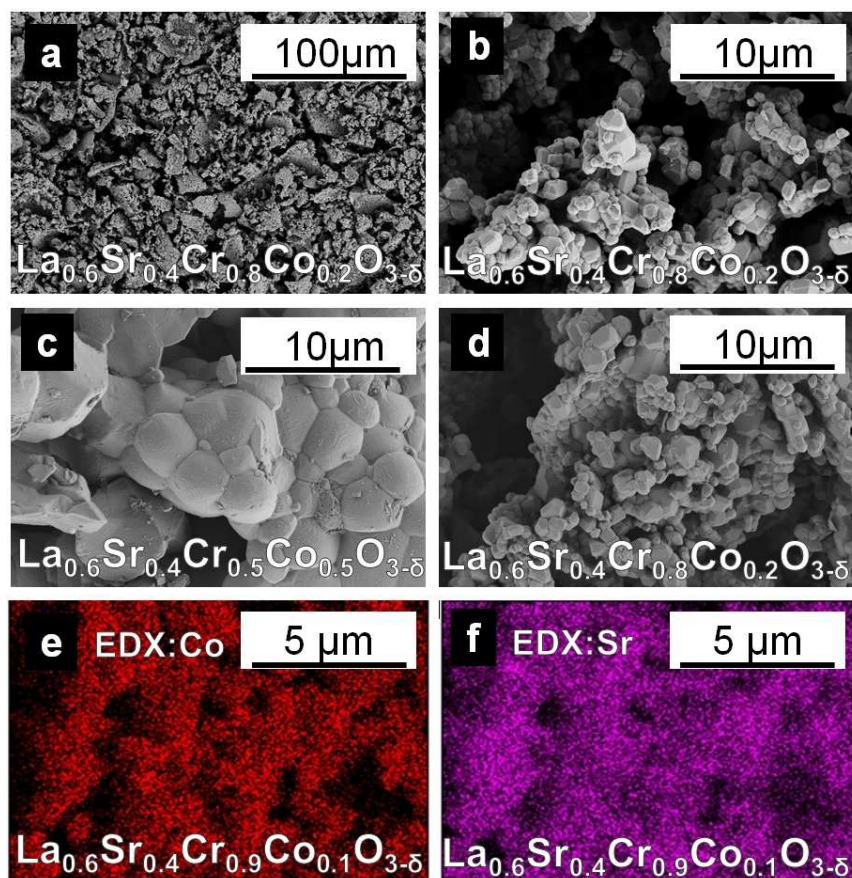


Figure 5. Scanning electron microscopy and energy dispersive X-ray (EDX) pictures of $\text{La}_{0.6}\text{Sr}_{0.4}\text{Cr}_{1-x}\text{Co}_x\text{O}_{3-\delta}$ for $x=0.05, 0.10, 0.20,$ and 0.50 . Images a,b) show the microstructure of the as-synthesized powders for two different magnifications. c) and d) display the powders $\text{La}_{0.6}\text{Sr}_{0.4}\text{Co}_{0.5}\text{O}_{3-\delta}$ and $\text{La}_{0.6}\text{Sr}_{0.4}\text{Co}_{0.2}\text{O}_{3-\delta}$ respectively after thermochemical cycling. e) and f) reveal the (EDX) pictures of thermochemically cycled $\text{La}_{0.6}\text{Sr}_{0.4}\text{Co}_{0.1}\text{O}_{3-\delta}$ of strontium and cobalt respectively. Difference in concentrations of Sr and Co reflect the morphology of the sample.

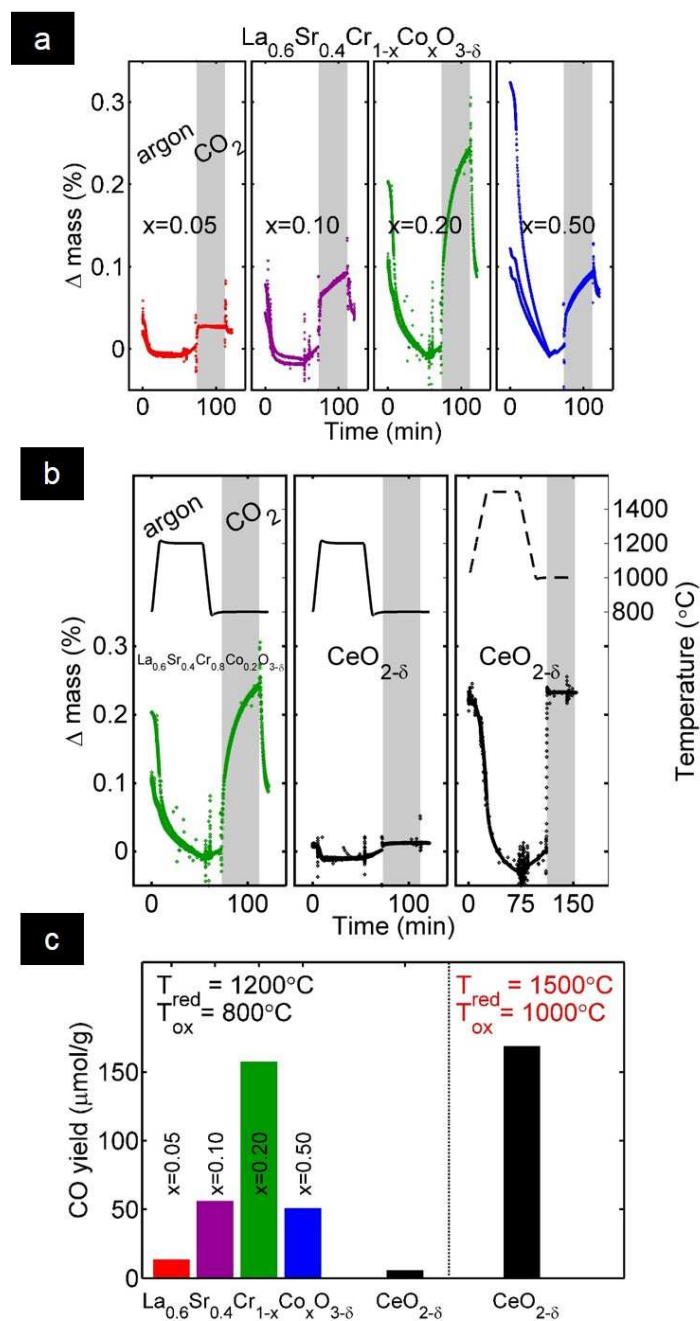


Figure 6. Thermogravimetric analysis of $\text{La}_{0.6}\text{Sr}_{0.4}\text{Cr}_{1-x}\text{Co}_x\text{O}_{3-\delta}$ and CeO_2 for reduction in argon and re-oxidation with CO_2 . a) Impact on CO_2 -splitting performance with cobalt substitution in $\text{La}_{0.6}\text{Sr}_{0.4}\text{Cr}_{1-x}\text{Co}_x\text{O}_{3-\delta}$ for a 1200-800 $^{\circ}\text{C}$ cycle. 4 thermochemical cycles were performed and here reproducible cycles 2-4 are depicted. b) Performance comparison of $\text{La}_{0.6}\text{Sr}_{0.4}\text{Cr}_{0.8}\text{Co}_{0.2}\text{O}_{3-\delta}$ and pure ceria. Ceria is compared for the same conditions and for a higher operating temperature cycle 1500-1000 $^{\circ}\text{C}$, higher temperature cycle profile is displayed with a dashed line. c) Average quantity of CO released in 3 subsequent thermochemical cycles for $\text{La}_{0.6}\text{Sr}_{0.4}\text{Cr}_{1-x}\text{Co}_x\text{O}_{3-\delta}$ and state-of-the material CeO_2 for the same temperature cycle as the perovskite, and a temperature cycle of 1500-1000 $^{\circ}\text{C}$.

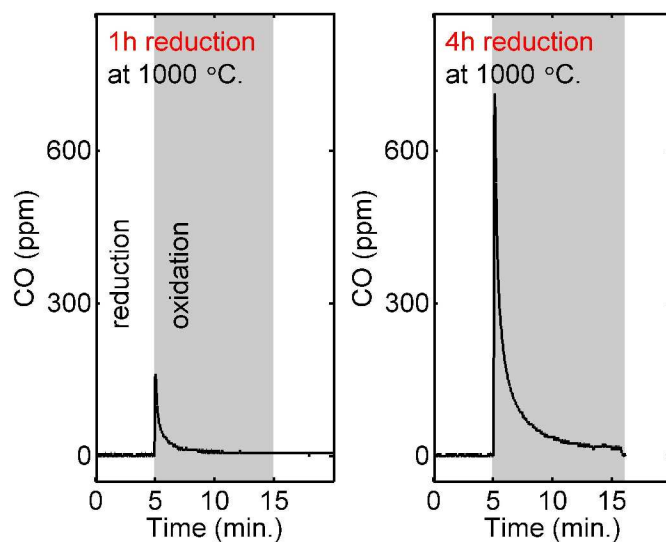


Figure 7. Carbon monoxide production measured by NDIR detector for $\text{La}_{0.6}\text{Sr}_{0.4}\text{Cr}_{0.8}\text{Co}_{0.2}\text{O}_{3-\delta}$ by splitting CO_2 in a fluidized bed reactor in a temperature cycle of 800 to 1000°C. The material was reduced at 1000°C for 1 h and 4 h in the first and second cycle respectively before it was re-oxidized by CO_2 at 800°C. CO production yields are 10 and 63 $\mu\text{mol/g}$ for the short and longer reduction cycle respectively.

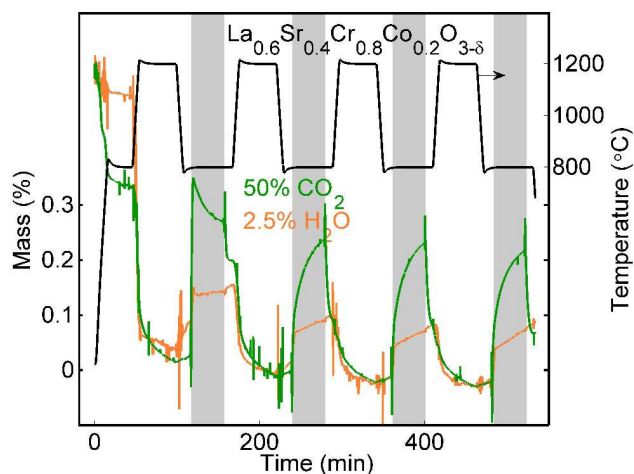


Figure 8. Thermogravimetric cycling data of $\text{La}_{0.6}\text{Sr}_{0.4}\text{Cr}_{0.8}\text{Co}_{0.2}\text{O}_{3-\delta}$ for two experiments with reduction in argon and re-oxidation with either 50% CO_2 or 2.5% H_2O in argon. Outliers are artefacts arising as a consequence of the high sensitivity of the thermogravimetric analyser. Reproducible cycles are observed for cycle 2-4 for re-oxidation with both water and carbon dioxide.

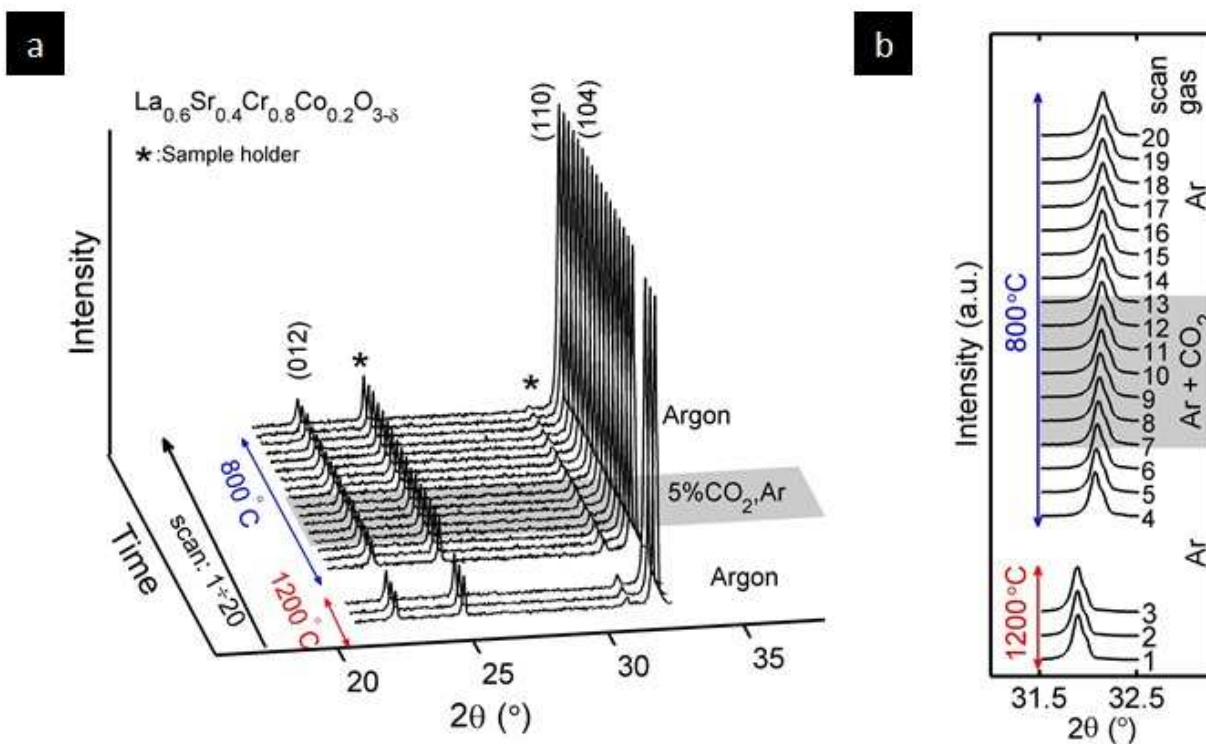


Figure 9. In-situ X-ray powder diffraction patterns of $\text{La}_{0.6}\text{Sr}_{0.4}\text{Cr}_{0.8}\text{Co}_{0.2}\text{O}_{3-\delta}$ for different temperatures and atmospheric conditions relevant for solar-to-fuel conversion: High temperature reducing step (patterns 1–3) was performed at 1200°C in argon atmosphere. After cooling down to 800°C and equilibration in argon atmosphere (patterns 4–6) the sample is exposed to oxidizing conditions with 5 vol% CO_2 mixed in argon (patterns 7–13, oxidizing conditions marked with grey patch). Finally the sample was kept in reducing argon atmosphere still at 800°C (patterns 14–20). a) 2θ range of 20–33° shows no phase separation or carbonate formation between peaks (012) and the doublet (110) and (104). Additional peaks marked with asterisk symbol (*) are related to the alumina sample holder. b) Narrow range to enhance the shape of the strong doublet for the peaks (110) and (104). Slight shift of the peak position can be related to the chemical expansion.